Available online at www.sciencedirect.com
ScienceDirect
Comput. Methods Appl. Mech. Engrg. 285 (2015) 829–848
Computer methods in applied mechanics and engineering
www.elsevier.com/locate/cma

An integrated fast Fourier transform-based phase-field and crystal plasticity approach to model recrystallization of three dimensional polycrystals

L. Chen[a,*], J. Chen[b], R.A. Lebensohn[c], Y.Z. Ji[a], T.W. Heo[a,1], S. Bhattacharyya[a,2], K. Chang[a,3], S. Mathaudhu[d], Z.K. Liu[a], L.-Q. Chen[a]

[a] *Department of Materials Science and Engineering, Pennsylvania State University, University Park, PA 16802, USA*
[b] *Department of Engineering, Pennsylvania State University, The Altoona College, Altoona, PA 16601, USA*
[c] *Materials Science and Technology Division, Los Alamos National Laboratory, Los Alamos, NM 87845, USA*
[d] *Materials Science Division, U.S. Army Research Office, Research Triangle Park, NC 27709, USA*

Received 19 April 2014; received in revised form 1 December 2014; accepted 3 December 2014
Available online 16 December 2014

Abstract

A fast Fourier transform (FFT) based computational approach integrating phase-field method (PFM) and crystal plasticity (CP) is proposed to model recrystallization of plastically deformed polycrystals in three dimensions (3-D). CP at the grain level is employed as the constitutive description to predict the inhomogeneous distribution of strain and stress fields after plastic deformation of a polycrystalline aggregate while the kinetics of recrystallization is obtained employing a PFM in the plastically deformed grain structure. The elasto-viscoplastic equilibrium is guaranteed during each step of temporal phase-field evolution. Static recrystallization involving plasticity during grain growth is employed as an example to demonstrate the proposed computational framework. The simulated recrystallization kinetics is compared using the classical Johnson–Mehl–Avrami–Kolmogorov (JMAK) theory. This study also gives us a new computational pathway to explore the plasticity-driven evolution of 3D microstructures.
Published by Elsevier B.V.

Keywords: Phase-field method; Crystal plasticity; Grain growth; Recrystallization

1. Introduction

Microstructure plays a crucial role in determining the properties of polycrystalline materials, which therefore stimulated enormous efforts to tailor the microstructure of polycrystals by a combination of thermal and mechanical processes. One widely used process is static recrystallization (SRX) by annealing of plastically deformed grain

* Corresponding author. Tel.: +1 814 777 6248.
E-mail address: luc28@psu.edu (L. Chen).

[1] Current address: Lawrence Livermore National Laboratory, 7000 East Avenue, Livermore, CA 94550, USA.

[2] Current address: Department of Materials Science and Engineering, Indian Institute of Technology Hyderabad, Ordnance Factory Campus, Yeddumailaram 502205, Andhra Pradesh, India.

[3] Current address: Korea Atomic Energy Research Institute; 1045 Daedeo kdaero, Yuseong-gu, Daejeon, 305-353, Republic of Korea.

http://dx.doi.org/10.1016/j.cma.2014.12.007
0045-7825/Published by Elsevier B.V.

structures [1,2]. The kinetics of recrystallization, i.e. the volume fraction of recrystallized grains as a function of time, is often described by the Johnson–Mehl–Avrami–Kolmogorov (JMAK) model [3,4] based on the assumptions that the nucleation rate is constant or the number of nucleation sites is fixed, constant growth velocity, and spherical grain shapes until impingement. JMAK theory assumes a homogeneous deformed state with a constant driving force and does not provide the microstructural details during recrystallization. To overcome these shortcomings, numerous attempts have been made to model the recrystallization process using meso-scale computational methods such as Monte Carlo Potts model [5–7] cellular automata model [8,9] and isogeometric method [10,11] to take into account the evolution of grain structures during recrystallization.

On the other hand, phase-field method (PFM) has been widely applied to model various meso-scale phenomena, e.g. solidification [12,13], solid-state transformation [14], recrystallization [15–18] and grain growth [19–21]. It can easily handle time-dependent growth geometries and describe complex microstructure morphologies, which make it particularly suitable for modeling microstructure evolution where morphological complexities are common. However, most of existing PFMs incorporate the strain energy contribution to microstructure evolution in the elastic regime. Both experimental and computational results have shown that the stresses in the context of polycrystals or microstructures can significantly exceed the elastic limit. Therefore, a PFM including not only the driving forces originating from the elastic fields, but also the driving forces resulting from the plastic activities is necessary for modeling microstructure evolution.

Plastic deformation can be introduced in two different ways in the context of PFM. Since plasticity in crystals is primarily due to the generation and motion of dislocations, one approach is to explicitly introduce mobile dislocations [22–24] using continuous fields for each slip system. In this approach, it is necessary to resolve the dislocation core size using several numerical grid spacing. In this case, the description of a realistic dislocation core size, which is important for the short-range interaction between dislocations, would require a very refine grid size [23]. Therefore, the spatial length scale in this approach is limited, and large scale simulations are computationally expensive. In addition, plastic deformation mechanisms other than dislocation glide (e.g. climb and/or cross-slip at high temperatures, or twining in materials with law stacking-fault energy) are not included in this approach.

Another approach is to directly include a plastic strain field defined at the meso-scale in PFM [25]. For example, Boussinot et al. [26] employs a decrease in the lattice misfit to account for the plastic activity. Zhou et al. [27] relates the plastic strain to the inter-dislocation distance, i.e. the dislocation density. In particular, the crystal plasticity (CP) theory has been rigorously formulated [28] and extensively used to obtain the micromechanical response of plastically deforming polycrystalline aggregates.

A number of efforts have made to couple PFM and plasticity theory at the meso-scale. The first attempt to couple PFM with an isotropic plasticity model was proposed by Guo et al. [29], who investigated the stress fields around defects such as holes and cracks. Later, Ubachs et al. [30] proposed a general formalism to incorporate phase-field and isotropic viscoplasticity with non-linear hardening for investigating tin–lead solder joints undergoing thermal cycling. Subsequently, similar approaches have been introduced to study crystal growth [31], martensites [32], superalloys [27,33] and diffusion controlled growth kinetics [34,35].

There have also been attempts to employ the PFM integrating plasticity to simulate the recrystallization, either in the context of a dislocation density based plastic model [15], or in a CP framework, including both hardening and viscosity [8,16]. For example, Takaki et al.'s model [15] assumed a homogeneous dislocation density field in each grain. However, ignoring the intragranular heterogeneity may lead to a poor representation of recrystallization kinetics and microstructure evolution. On the other hand, a successful PFM/CP coupling depends, to a large extent, on the availability of efficient, and yet reliable, CP implementations. In this sense, while the finite element method (FEM) has been extensively used to deal with problems involving CP (for an excellent review on CP-FEM, see [28]), the large number of degrees of freedom required by such CP-FEM calculations limits the size of the aggregates that can be investigated by this method.

Conceived as an alternative to CP-FEM, a formulation inspired by image-processing techniques and based on the spectral FFT algorithm has been recently proposed to predict the micromechanical behavior of plastically deforming heterogeneous polycrystals [36–40]. Owing to being free from any large matrix inversion, this spectral FFT formulation is very computationally efficient. It is numerically demonstrated that the computational time of the CP-FEM solver is about 25–40 times more than that of the CP-FFT counterpart when achieving the same level of fidelity [41]. Such cheap computation makes the FFT solver an excellent candidate to incorporate fine-scale microstructural information in plastic deformation simulations.

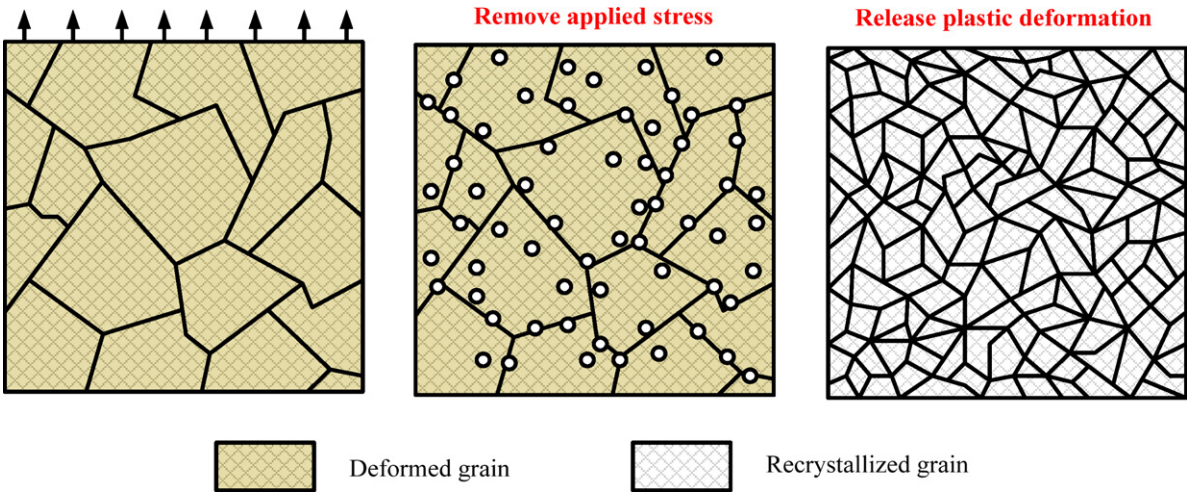

Fig. 1. Schematic diagram showing a typical static recrystallization process.
Source: This figure is adapted from Wikimedia Commons.

In this paper, we propose to couple our previous FFT-based PFM [19,20] and the CP-FFT model [36–40], by taking advantage of the high efficiency in the FFT solver, to model the recrystallization of plastically deformed polycrystalline materials in 3-D. In this approach, the plastic strain field is first calculated with the CP-FFT approach for its subsequent use by the FFT-based PFM for the determination of the driving forces for recrystallization. The use of the FFT algorithm in both PFM and CP not only guarantees their seamless integration from a numerical perspective, but also helps us to significantly enhance the computational efficiency. The elasto-viscoplastic equilibrium is solved during each step of temporal phase-field evolution. The proposed computational framework is applicable to other plasticity-driven phase-field evolution processes.

The plan of the paper is as follows: in Section 2 we summarize the essential aspects of the FFT-based CP model and present how elastic equilibrium for each step of phase-field evolution is solved. Next, Section 3 describes the formulation of the PFM for static recrystallization of plastically deformed polycrystals, paying special attention to the determination of the plastic driving forces. Examples of phase-field simulation of recrystallization process are described in Section 4, where a simply case with only one deformed crystal is designed to validate the recrystallization kinetics of the proposed model, followed by a realistic case with multiple deformed grains. Finally, we draw our conclusions in Section 5.

2. FFT-based crystal plasticity (CP-FFT) model

The main purpose of this study is to integrate a FFT-based micro-elastic PFM with a CP-FFT model for simulating the phase-field evolution, using static recrystallization of plastically deformed polycrystals as an example. The procedure of static recrystallization is schematically illustrated in Fig. 1: (1) a sufficiently high level of stress is applied to a polycrystalline material, producing plastic deformation. At single crystal level, plastic deformation results in energy storage in each grain in the form of dislocations; (2) the applied stress is then released, followed by heating of the deformed polycrystal to an elevated temperature; and (3) the plastic energy drives the nucleation and growth of recrystallized grains, restoring the heavily deformed grains to a low dislocation density state.

The first step of the static recrystallization model is to compute the plastic deformation of polycrystals and the corresponding plastically stored energy distribution. In the proposed method, the CP-FFT model with full-field formulations is employed for this purpose.

2.1. Starting microstructure

The initial polycrystalline structures, as illustrated in Fig. 2(a), can be easily generated from our real-space phase-field grain growth simulations [20], in which the grain size can be controlled. Alternatively, an experimentally determined image of the microstructure of interest can be directly utilized as the input to the present model [39]. It is

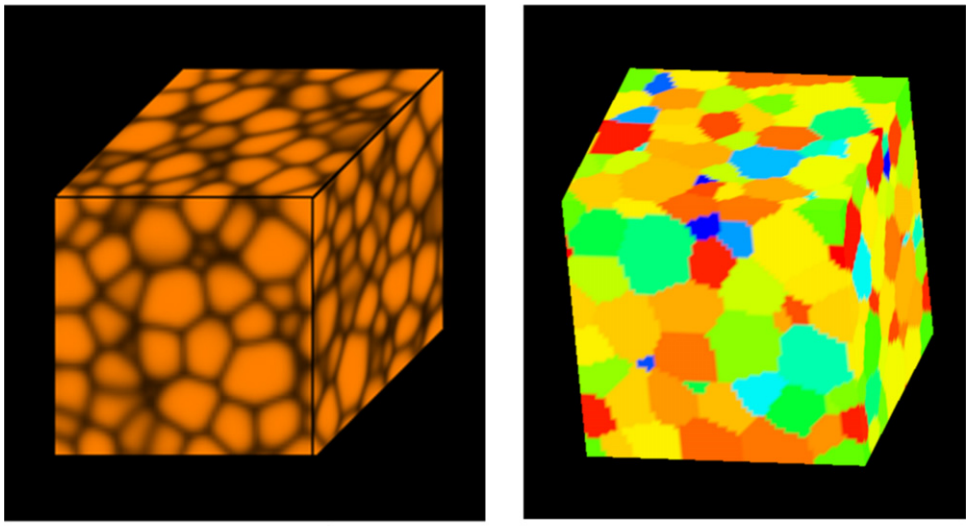

Fig. 2. Starting 3-D microstructure used in the simulations.

worth noting that because of the continuous variation of order parameters, grain boundaries in the phase-field are diffuse [14], whereas the counterparts in CP-FFT model are infinitely sharp, as shown in Fig. 2(b). A simple but effective numerical means to achieve the transformation between microstructures with diffuse and sharp grain boundaries will be detailed in Section 3.2.1.

2.2. Viscoplastic FFT-based formulation

The FFT-based formulation for viscoplastic polycrystals has been described in detail in previous papers [36–40]. Therefore, here we only provide the essential aspects of the method. The interested readers are referred to previous publications for further details.

The micromechanical fields that develop during plastic deformation in polycrystalline aggregates can be obtained as an extension of the spectral method originally proposed by [42] for linear and non-linear composites. The FFT-based formulation provides an exact solution of the governing equations in a periodic unit cell, adjusting iteratively a strain-rate field, associated with a kinematically-admissible velocity field, which minimizes the average of local work-rate, under the compatibility and equilibrium constraints. The method is based on the fact that the local mechanical response of a periodic heterogeneous medium can be calculated as a convolution integral between the Green function of a linear reference homogeneous medium and a polarization field, proportional to the actual heterogeneity and micromechanical fields. Since such type of integrals reduces to a simple product in Fourier space, FFT can be used to transform the polarization field into Fourier space and, in turn, to get the micromechanical fields by inverse-transforming that product back to Cartesian space. Given that the actual polarization field depends on *a priori* unknown fields, an iterative scheme is necessary to converge towards a compatible strain-rate field and an equilibrated stress field. However, the requirement of periodic boundary conditions in Fourier space makes the FFT-based formulation less general than the CP-FEM formulation. In order to ensure the computational efficiency, the small strain formulations are utilized to describe the constitutive relations and governing equations, without the multiplicative decomposition of the deformation gradient into elastic and plastic parts.

The periodic unit cell representing the polycrystal is discretized by means of a regular grid $\left\{\mathbf{x^d}\right\}$. A corresponding grid of the same dimensions, $\left\{\boldsymbol{\xi}^{\mathbf{d}}\right\}$, is used in Fourier space. Velocities and tractions along the boundary of the unit cell need to be determined. An average velocity gradient $V_{i,j}$ is imposed to the unit cell, which gives an average strain-rate $\dot{E}_{ij} = \frac{1}{2}\left(V_{i,j} + V_{j,i}\right)$. The local strain-rate field is a function of the local velocity field, i.e. $\dot{\varepsilon}_{ij}\left(v_k\left(\mathbf{x}\right)\right)$, and can be split into average and fluctuation terms, $\dot{\varepsilon}_{ij}\left(v_k\left(\mathbf{x}\right)\right) = \dot{E}_{ij} + \tilde{\dot{\varepsilon}}_{ij}\left(\tilde{v}_k\left(\mathbf{x}\right)\right)$, where $v_i\left(\mathbf{x}\right) = \dot{E}_{ij}x_j + \tilde{v}_i\left(\mathbf{x}\right)$.

The constitutive equation that relates the local deviatoric stress $\boldsymbol{\sigma}'(\mathbf{x})$ and the local strain-rate $\dot{\boldsymbol{\varepsilon}}(\mathbf{x})$ at point $\mathbf{x}$ is obtained by adding the contribution of the S slip systems active at single crystal level:

$$\dot{\boldsymbol{\varepsilon}}(\mathbf{x}) = \sum_{s=1}^{S} \mathbf{m}^s(\mathbf{x})\ \dot{\gamma}^s(\mathbf{x}) = \dot{\gamma}_o \sum_{s=1}^{S} \mathbf{m}^s(\mathbf{x}) \left(\frac{\mathbf{m}^s(\mathbf{x}) : \boldsymbol{\sigma}'(\mathbf{x})}{\tau^s(\mathbf{x})} \right)^n \times \operatorname{sgn}\left(\mathbf{m}^s(\mathbf{x}) : \boldsymbol{\sigma}'(\mathbf{x}) \right) \tag{1}$$

where $\mathbf{m}^s$ is the Schmid tensor of slip system (s) defined as $\mathbf{m}^s = (\mathbf{n}^s \otimes \mathbf{b}^s + \mathbf{b}^s \otimes \mathbf{n}^s)/2$ with $\mathbf{n}^s$ and $\mathbf{b}^s$ being the normal and Burgers vectors of system (s); $\dot{\gamma}^s$ and τ^s are, respectively, the shear-rate and critical stress of slip system (s); n is the stress exponent, and $\dot{\gamma}_o$ is a reference shear-rate. Note that Eq. (1) amounts to neglect elastic strains, which are assumed to be very small compared to plastic strains, at sufficiently large deformations.

The Cauchy stress field can be written as:

$$\boldsymbol{\sigma}(\mathbf{x}) = \mathbf{L}^o : \dot{\boldsymbol{\varepsilon}}(\mathbf{x}) + \boldsymbol{\varphi}(\mathbf{x}) - p(\mathbf{x})\ \mathbf{I} \tag{2}$$

where $p(\mathbf{x})$ is the hydrostatic pressure field, $\mathbf{L}^o$ is the stiffness of a linear reference medium, and $\varphi(\mathbf{x})$ is the polarization field, given by:

$$\boldsymbol{\varphi}(\mathbf{x}) = \boldsymbol{\sigma}'(\mathbf{x}) - \mathbf{L}^o : \dot{\boldsymbol{\varepsilon}}(\mathbf{x}). \tag{3}$$

Combining Eq. (2) with the equilibrium ($\sigma_{ij,j}(\mathbf{x}) = \mathbf{0}$), and incompressibility conditions:

$$\begin{vmatrix} L^o_{ijkl} v_{k,lj}(\mathbf{x}) + \varphi_{ij,j}(\mathbf{x}) - p_{,i}(\mathbf{x}) = 0 \\ v_{k,k}(\mathbf{x}) = 0 \end{vmatrix} \tag{4}$$

where we have used the relation: $\dot{\varepsilon}_{ij}(\mathbf{x}) = \frac{1}{2}\left(v_{i,j}(\mathbf{x}) + v_{j,i}(\mathbf{x}) \right)$. The system of differential equations (4), with periodic boundary conditions across the unit cell, can be solved by means of the Green function method. If G_{km} and H_m are the periodic Green functions associated with the velocity and hydrostatic pressure fields, the solutions of system (4) are convolution integrals between those Green functions and the polarization field. The velocity gradient, after some manipulation, is given by:

$$\tilde{v}_{i,j}(\mathbf{x}) = \int_{R^3} \mathrm{G}_{ik,jl}\left(\mathbf{x} - \mathbf{x}' \right)\ \varphi_{kl}\left(\mathbf{x}' \right)\ \mathrm{d}\mathbf{x}'. \tag{5}$$

Convolution integrals in direct space are simply products in Fourier space. Hence:

$$\hat{\tilde{\varepsilon}}_{ij}(\boldsymbol{\xi}) = \hat{\Gamma}^{sym}_{ijkl}(\boldsymbol{\xi})\ \hat{\varphi}_{kl}(\boldsymbol{\xi}) \tag{6}$$

where the symbol "$\wedge$" indicates the Fourier transform and $\Gamma^{sym}_{ijkl} = sym\left(G_{ik,jl}\right)$. The tensor $\hat{\Gamma}^{sym}_{ijkl}(\boldsymbol{\xi})$ is only function of $\mathbf{L}^o$ and can be readily obtained for every point belonging to $\left\{ \boldsymbol{\xi}^{\mathbf{d}} \right\}$ (for details, see [39]). The so-called FFT-based *basic scheme* [42] consists of: (1) inverse-transforming Eq. (6), to obtain a new guess for the strain-rate field, (2) with the latter, solving Eq. (1) to obtain the new guess for the stress field; (3) replacing those new estimations of the micromechanical fields in Eq. (3) to obtain the new polarization field, and so on and so forth, until reaching convergence.

Because of the strong mechanical contrast associated with the viscoplastic constitutive relation (Eq. (1)), the actual iterative procedure used in the simulations presented here employs the augmented Lagrangians algorithm [43,44], consisting of updating equilibrated stress and compatible strain-rate fields, along with two auxiliary stress and strain-rate fields related to each other by the constitutive relation (for details, see [39]). Upon convergence, the micromechanical fields and microstructure are updated incrementally, using an explicit scheme. For example, the strain-rate field calculated at time t is assumed to be constant during a time interval $[t,\ t + \Delta t]$ and the total macroscopic and local strains are then calculated as: $E^{(t+\Delta t)}_{ij} = E^{(t)}_{ij} + \dot{E}_{ij} \times \Delta t$ and $\varepsilon^{(t+\Delta t)}_{ij}(x) = \varepsilon^{(t)}_{ij}(x) + \dot{\varepsilon}_{ij}(x) \times \Delta t$, respectively. For further use, let us call:

$$\boldsymbol{\varepsilon}^p(\mathbf{x}) = \boldsymbol{\varepsilon}^{(\mathrm{t_F})}(\mathbf{x}) \quad \text{and} \quad \varepsilon^p_{vM}(\mathbf{x}) = \sqrt{\frac{2}{3}\boldsymbol{\varepsilon}^p(\mathbf{x}) : \boldsymbol{\varepsilon}^p(\mathbf{x})} \tag{7}$$

where t_F is the final time, i.e. at which the application of plastic deformation onto the polycrystal is completed.

The local crystallographic orientations are updated according to the following local lattice rotation-rate:

$$\boldsymbol{\omega}(\mathbf{x}) = \left(\dot{\boldsymbol{\Omega}} + \tilde{\dot{\boldsymbol{\omega}}}(\mathbf{x}) - \dot{\boldsymbol{\omega}}^{p}(\mathbf{x})\right) \times \Delta t \tag{8}$$

where: $\dot{\Omega}_{ij} = \frac{1}{2}\left(V_{i,j} - V_{j,i}\right)$ is the antisymmetric part of the macroscopic velocity gradient; $\dot{\boldsymbol{\omega}}^{p}(\mathbf{x})$ is the plastic spin obtained as:

$$\dot{\boldsymbol{\omega}}^{p}(\mathbf{x}) = \sum_{s=1}^{S} \boldsymbol{\alpha}^{s}(\mathbf{x})\, \dot{\gamma}^{s}(\mathbf{x}) \tag{9}$$

with $\boldsymbol{\alpha}^{s}(\mathbf{x}) = \frac{1}{2}\left(\mathbf{n}^{s}(\mathbf{x}) \otimes \mathbf{b}^{s}(\mathbf{x}) - \mathbf{b}^{s}(\mathbf{x}) \otimes \mathbf{n}^{s}(\mathbf{x})\right)$ being the antisymmetric Schmid tensor associated with slip system s; and $\tilde{\dot{\boldsymbol{\omega}}}(\mathbf{x})$ is the local fluctuation in rigid-body rotation-rate, obtained by inverse-transforming the converged anti-symmetric field:

$$\hat{\tilde{\dot{\boldsymbol{\omega}}}}\left(\mathbf{x}^{d}\right) = fft^{-1}\left\{\hat{\boldsymbol{\Gamma}}^{antisym}\left(\boldsymbol{\xi}^{\mathbf{d}}\right) : \hat{\varphi}\left(\boldsymbol{\xi}^{\mathbf{d}}\right)\right\}. \tag{10}$$

Finally, the field of critical resolved shear stresses $\tau^{s}(\mathbf{x})$ is also updated after each deformation increment. Adopting a simple linear hardening, the hardening rate for all systems is given by:

$$\dot{\tau}^{s}(\mathbf{x}) = H\dot{\Gamma}(\mathbf{x}) \tag{11}$$

where H is the hardening coefficient and $\dot{\Gamma}(\mathbf{x}) = \sum_{s=1}^{S} |\dot{\gamma}^{s}(\mathbf{x})|$ is the total shear-rate.

2.3. Recrystallization nucleation

In general, there are two main recrystallization nucleation mechanisms depending on the dislocation behaviors. One is based on the coarsening of subgrains which originates from the dislocation networks in the dynamic recovery of plastically deformed microstructures, corresponding to high stacking-fault energy materials (e.g. Aluminum). Another mechanism is strain induced grain boundary migration (SIBM) on a more phenomenological basis, corresponding to low stacking-fault energy materials (e.g. Copper). SIBM involves the bulging of part of a pre-existing grain boundary, leaving a dislocation-free region behind the migrating boundary [2].

The SIBM nucleation mechanism is chosen in this study based on site-saturated nucleation conditions for simplicity. Specifically, the model assumes that nucleation occurs only at locations with a von Mises plastic strain $\varepsilon^{p}_{vM}(\mathbf{x})$ exceeding a critical value $\varepsilon^{p}_{crit}(\mathbf{x})$:

$$\varepsilon^{p}_{vM}(\mathbf{x}) > \varepsilon^{p}_{crit}(\mathbf{x}). \tag{12}$$

It is worth noting that such plastic strain-based nucleation criterion is different from the dislocation density-based nucleation criterion, since the high plastic sites within grains possibly do not have high dislocation density.

These recrystallization nuclei are introduced as small grains into the computational domain. At these locations, the nuclei are created with random orientation attributes, whereas the local plastic strain is reset to zero. In addition to the above criteria, we set the distance between two neighboring nuclei to be more than 5 grids, because the PFM uses the diffusive interface region with a finite width. Next, if the conditions are appropriate, i.e. if its boundaries have enough mobility and sufficiently large driving force to move, a recrystallized nucleus may sweep a deformed neighbor grain, advancing in this way the recrystallization process.

2.4. FFT-based equilibrium after each phase-field temporal step

The second step of the proposed model is to simulate the growth of recrystallized grains. An important condition for the simulation of this process is the fulfillment of stress equilibrium. Due to the annealing of plastic deformation in the recrystallized regions, the elastic strains have been found to become comparable with the corresponding plastic strains. Consequently, in order to fulfill static mechanical equilibrium during the PFM simulation, the plastic strain field $\boldsymbol{\varepsilon}^{p}(\mathbf{x})$, whose initial value for the PFM is given by Eq. (7) and whose evolution is determined by the nucleation and growth of recrystallized regions with $\boldsymbol{\varepsilon}^{p}(\mathbf{x}) = \sum_{g} H(\eta_{g}(\mathbf{x}))\boldsymbol{\varepsilon}^{p}_{g}(\mathbf{x})$ (detailed in Section 3.2.2), is considered as

an eigenstrain field. The FFT-based solution of this problem is then solved by the formulations for stress equilibrium proposed by [19,45,46].

In the case of the presence of an eigenstrain field $\boldsymbol{\varepsilon}^p_{ij}(\mathbf{x})$, the total strain field is:

$$\boldsymbol{\varepsilon}(\mathbf{x}) = \boldsymbol{\varepsilon}^e(\mathbf{x}) + \boldsymbol{\varepsilon}^p(\mathbf{x}). \tag{13}$$

The elastic strain field $\boldsymbol{\varepsilon}^e(\mathbf{x})$ is linearly related to stress:

$$\boldsymbol{\sigma}(\mathbf{x}) = \mathbf{C}(\mathbf{x}) : \boldsymbol{\varepsilon}^e(\mathbf{x}) = \mathbf{C}(\mathbf{x}) : \left(\boldsymbol{\varepsilon}(\mathbf{x}) - \boldsymbol{\varepsilon}^p(\mathbf{x})\right). \tag{14}$$

Similarly to Eq. (2) in the viscoplastic case, the use of a homogeneous elastic stiffness $\mathbf{C}^o$ allows us to rewrite Eq. (14) as:

$$\boldsymbol{\sigma}(\mathbf{x}) = \mathbf{C}^o : \boldsymbol{\varepsilon}(\mathbf{x}) + \boldsymbol{\varphi}(\mathbf{x}). \tag{15}$$

In this case, the polarization field is given by:

$$\boldsymbol{\varphi}(\mathbf{x}) = \boldsymbol{\sigma}(\mathbf{x}) - \mathbf{C}^o : \boldsymbol{\varepsilon}(\mathbf{x}) = \left(\mathbf{C}(\mathbf{x}) - \mathbf{C}^o\right) : (\mathbf{E} + \tilde{\boldsymbol{\varepsilon}}(\mathbf{x})) - \mathbf{C}(\mathbf{x}) : \boldsymbol{\varepsilon}^p(\mathbf{x}). \tag{16}$$

Enforcing equilibrium: $\sigma_{ij,j}(\mathbf{x}) = \mathbf{0}$, we obtain:

$$C^o_{ijkl}\, u_{k,lj}(\mathbf{x}) + \varphi_{ij,j}(\mathbf{x}) = 0 \tag{17}$$

where $u_k(\mathbf{x})$ is the displacement field and $\varepsilon_{ij}(\mathbf{x}) = \frac{1}{2}\left(u_{i,j}(\mathbf{x}) + u_{j,i}(\mathbf{x})\right)$. The Green's function method is again used to solve this system of differential equations. If $G_{km}(\mathbf{x})$, the Green's function associated with the displacement field, can be determined, the solution of Eq. (17) is given by:

$$u_k(\mathbf{x}) = \int_{R^3} G_{ki,j}(\mathbf{x} - \mathbf{x}')\varphi_{ij}(\mathbf{x}')d\mathbf{x}'. \tag{18}$$

Taking gradient of Eq. (18) and expressing the resulting convolution integral in Fourier space gives:

$$\hat{\tilde{u}}_{i,j}(\boldsymbol{\xi}) = \hat{\Gamma}_{ijkl}(\boldsymbol{\xi})\ \hat{\varphi}_{kl}(\boldsymbol{\xi}) \tag{19}$$

where $\Gamma_{ijkl} = G_{ik,jl}$. These operators are calculated in Fourier space as: $\hat{G}_{ij}(\boldsymbol{\xi}) = A^{-1}_{ij}(\boldsymbol{\xi})$ where $A_{ij}(\boldsymbol{\xi}) = \xi_j\xi_l C^o_{ijkl}$, and $\hat{\Gamma}_{ijkl}(\boldsymbol{\xi}) = -\xi_j\xi_l\hat{G}_{ij}(\boldsymbol{\xi})$. Anti-transforming and symmetrizing Eq. (19), a new guess for the total strain fluctuation field $\tilde{\boldsymbol{\varepsilon}}(\mathbf{x})$ is obtained. If the macroscopic strain E_{ij} is known, Eq. (16) gives a new guess of the polarization field, and so on and so forth, until the input total strain field coincides with the output field within a certain tolerance.

While the above algorithm corresponds to a macroscopic strain applied to the unit cell, static recrystallization problems typically correspond to macroscopic stress-free states. In this case, the macroscopic strain field should also be adjusted iteratively after each iteration (i) according to [44]:

$$\mathbf{E}^{(i+1)} = \left\langle \boldsymbol{\varepsilon}^{(i)}(\mathbf{x}) \right\rangle - \mathbf{C}^{o^{-1}} : \left\langle \boldsymbol{\sigma}^{(i)}(\mathbf{x}) \right\rangle \tag{20}$$

where $\langle\cdot\rangle$ indicates average over the entire Fourier grid.

3. Phase-field method

In the phase-field method, each point of a polycrystalline microstructure is described by continuous and non-conservative order parameters $\eta_g(\mathbf{x}, t)$ $(g = 1..G)$. Within the interior of each grain only one of the order parameters adopts the value of unity, and the rest of the order parameters have the value of zero. Thus, each order parameter represents the unique crystallographic orientation of a grain. The order parameter values continuously change from 1 to 0 across the grain boundary [14].

The PFM and the FFT-based CP model is coupled to model the microstructure evolution during static recrystallization, as shown in Fig. 1. During this process, the deformed and recrystallized grains coexist at equilibrium. In order to differentiate between these two types of grains, a new set of non-conservative order parameters $\phi_r(\mathbf{x}, t)$ $(r = 1..R)$ are introduced to account for the recrystallized grains, in addition to $\eta_g(\mathbf{x}, t)$ $(g = 1..G)$ describing the deformed grains.

The main ingredient of the PFM is a mesoscopic free-energy functional $\mathcal{F}$ relating the order parameters to the total free energy. It is usually decomposed into several contributions: chemical free energy (including a gradient term) and elastic energy $\mathcal{F}_{el}$, detailed in the next subsections. In the present case, the free energy functional also contain a plastic contribution $\mathcal{F}_{vp}$. Hence:

$$\mathcal{F} = \mathcal{F}_{ch}(\eta_g,\ \phi_r) + \mathcal{F}_{el}(\eta_g,\ \phi_r,\ \boldsymbol{\varepsilon}^{el}) + \mathcal{F}_{vp}(\eta_g,\ \boldsymbol{\varepsilon}^{p}) + \mathcal{F}^r_{ch}(\eta_g, \phi_r) + \mathcal{F}^r_{el}(\eta_g,\ \phi_r,\ \boldsymbol{\varepsilon}^{el}) \tag{21}$$

where $\mathcal{F}_{ch}$ is the chemical free energy. The superscript r denotes the energy contributions from the recrystallized grains, while the terms without supra-index indicate their counterparts from deformed grains. Note that due to the assumption of dislocation-free recrystallized grains, there is no plastic energy contribution from these grains.

3.1. Chemical free energy

Based on our previous phase-field grain growth model [14,19,20], the chemical free energy of a polycrystalline microstructure is expressed as:

$$\mathcal{F}_{ch} = \int_V \left[f_0(\eta_g,\ \phi_r) + \sum_{g=1}^{G} \frac{\kappa}{2} (\nabla \eta_g(\mathbf{x}, t)^2) \right] dV \tag{22}$$

$$\mathcal{F}^r_{ch} = \int_V \left[f^r_0(\eta_g,\ \phi_r) + \sum_{r=1}^{R} \frac{\kappa}{2} (\nabla \phi_r(\mathbf{x}, t)^2) \right] dV \tag{23}$$

where κ is a positive gradient coefficient associated with the gradients, and $f_0(\eta_q,\ \phi_r)$ and $f^r_0(\eta_q,\ \phi_r)$ are the local free energy densities of deformed and recrystallization grains, respectively, which are defined as:

$$\begin{aligned} f_0(\eta_g, \phi_r) \ =\ & -\frac{\alpha}{2} \sum_{g=1}^{G} \eta_q^2(\mathbf{x}, t) + \frac{\beta}{4} \left(\sum_{g=1}^{G} \eta_g^2(\mathbf{x}, t) \right)^2 \\ & + \left(\gamma - \frac{\beta}{2} \right) \left(\sum_{g=1}^{G} \sum_{s>g}^{G} \eta_g^2(\mathbf{x}, t) \eta_s^2(\mathbf{x}, t) \right) + \gamma \sum_{g=1}^{G} \sum_{r=1}^{R} \eta_g^2(\mathbf{x}, t) \phi_r^2(\mathbf{x}, t) \end{aligned} \tag{24}$$

$$\begin{aligned} f^r_0(\eta_g, \phi_r) \ =\ & -\frac{\alpha}{2} \sum_{r=1}^{R} \phi_r^2(\mathbf{x}, t) + \frac{\beta}{4} \left(\sum_{r=1}^{R} \phi_r^2(\mathbf{x}, t) \right)^2 \\ & + \left(\gamma - \frac{\beta}{2} \right) \left(\sum_{r=1}^{R} \sum_{s>r}^{R} \phi_r^2(\mathbf{x}, t) \phi_s^2(\mathbf{x}, t) \right) + \gamma \sum_{g=1}^{G} \sum_{r=1}^{R} \eta_g^2(\mathbf{x}, t) \phi_r^2(\mathbf{x}, t) \end{aligned} \tag{25}$$

where α, β and γ are constants, with $\alpha = \beta > 0$ and $\gamma > \beta/2$.

The local free energy density has $2(G + R)$ degenerate minima located at $(\eta_1, \eta_2, \ldots, \eta_G, \phi_1, \phi_2, \ldots, \phi_R) = (\pm 1, 0, \ldots, 0), (0, \pm 1, \ldots, 0), \ldots, (0, 0, \ldots, \pm 1)$. The minima associated with η_g or $\phi_r = -1$ are eliminated by setting the value of each order parameter equal to its absolute value during the initial stages of the simulation. This is required to prevent the variation of η_g or ϕ_r from $+1$ to -1 or vice-versa across a grain boundary which may lead to different grain boundary energy and mobility. To simulate the ideal case of grain growth we consider grain boundaries across which η_g or ϕ_r smoothly varies from 1 to 0 or vice versa.

3.2. Plastic energy

3.2.1. PFM/CP-FFT microstructure mapping

Owing to the continuous variation of properties, grain boundaries in the PFM are diffuse, rather than infinitely sharp, as in the CP-FFT model. In such case, a number of non-zero order parameters describe each material point in the PFM diffuse microstructure, as opposed to the CP-FFT sharp microstructure in which each material point corresponds to only one grain. In order to integrate both models, the following algorithm is designed to transform between the two microstructures:

(1) The PFM diffuse microstructure is transformed to a CP-FFT sharp one, by finding the dominant or *primary* order parameter (i.e. that with the maximum value) for each point in the diffuse microstructure, to be denoted $\eta_{prim}(\mathbf{x})$:

$$\eta_{prim}(\mathbf{x}) = \max\left[\eta_1(\mathbf{x}), \eta_2(\mathbf{x}), \ldots, \eta_G(\mathbf{x})\right] \tag{26}$$

and treating the grain that $\eta_{prim}(\mathbf{x})$ represents, as the one associated with the specific point $\mathbf{x}$ in the CP-FFT sharp microstructure.

(2) The plastic strains calculated with the CP-FFT model for the sharp microstructure are then employed to construct the plastic strain field to be mapped onto the PFM diffuse microstructure. Similar to the classic variable description in PFM, the plastic strain field $\boldsymbol{\varepsilon}^p_{PFM}(\mathbf{x})$ at point $\mathbf{x}$ is given in terms of its set of order parameters $\eta_g(\mathbf{x})$ $(g = 1..G)$ as:

$$\boldsymbol{\varepsilon}^p_{PFM}(\mathbf{x}) = \sum_g H(\eta_g(\mathbf{x}))\boldsymbol{\varepsilon}^p_{g,PFM}(\mathbf{x}) \tag{27}$$

where $\boldsymbol{\varepsilon}^p_{g,PFM}(\mathbf{x})$ is the plastic strain associated to g-th order parameter at point $\mathbf{x}$. An issue that needs to be addressed is that the plastic strains $\boldsymbol{\varepsilon}^p_{g,PFM}(\mathbf{x})$ hold a number of values for a number of order parameters for one specific point $\mathbf{x}$ in PFM, while the plastic strain $\boldsymbol{\varepsilon}^p_{FFT}(\mathbf{x})$ calculated with the CP-FFT model corresponds to the single grain associated with $\mathbf{x}$. Thus, in order to evaluate $\boldsymbol{\varepsilon}^p_{g,PFM}(\mathbf{x})$, we first calculate the averages $\boldsymbol{\varepsilon}^p_{g,FFT} = \left\langle \boldsymbol{\varepsilon}^p_{FFT}(\mathbf{x}) \right\rangle_g \forall g$ of the plastic strain field over all Fourier points belonging to each grain g in the entire CP-FFT computational domain. Next, since each point of the PFM diffuse microstructure is described by two types of order parameters: one *primary* and $G-1$ *secondary* order parameters, we compute $\boldsymbol{\varepsilon}^p_{g,PFM}(\mathbf{x})$ differently for both types:

(a) For the *primary* order parameter: $\boldsymbol{\varepsilon}^p_{g,PFM}(\mathbf{x}) = \boldsymbol{\varepsilon}^p_{FFT}(\mathbf{x})$, calculated by CP-FFT model for this specific point;

(b) For the *secondary* order parameters, $\boldsymbol{\varepsilon}^p_{g,PFM}(\mathbf{x}) = \boldsymbol{\varepsilon}^p_{g,FFT}$, as defined above.

Additionally, $H(\eta_g)$ in Eq. (27) is the interpolation function of grain parameters, and is defined as:

$$H(\eta_g) = -2\eta_g^3 + 3\eta_g^2 \tag{28}$$

which exhibits the following properties: (i) $H(\eta_g = 0) = 0$ and $H(\eta_g = 1) = 1$; (ii) $\partial H/\partial \eta_g|\eta_g = 0,\ 1 = 0$, thereby representing the artificial change in the equilibrium grain order parameter values within the bulk of each grain.

Similarly, the von Mises strain $\varepsilon_{vM}(\mathbf{x})$ of each material point (for later use) in PFM can be written as:

$$\varepsilon_{vM}(\mathbf{x}) = \sqrt{\frac{2}{3}\varepsilon^p_{ij}(\mathbf{x}) : \varepsilon^p_{ij}(\mathbf{x})} = \sum_g (-2\eta_g^3 + 3\eta_g^2)\varepsilon_{g,vM}(\mathbf{x}) \tag{29}$$

where the sub-index *PFM* is ignored for the purpose of simplification, and so are the rest subsections.

3.2.2. Plastic energy

The plastic energy in the framework of crystal plasticity is described classically with two variables related to the slip systems: the shear strain $\gamma^s(\mathbf{x},\ t)$ and the critical resolved shear stress $\tau^s(\mathbf{x},\ t)$ of slip system. They enter the accumulation of plastic energy from all the time steps in the CP-FFT calculation as follows:

$$\mathcal{F}_{vp} = \int_V f_{vp}\ (\mathbf{x})dV = \int_V \left[\int \Delta W_{vp}(\mathbf{x},\ t)dt\right] dV \tag{30}$$

where f_{vp} is the plastic energy density that is expressed by the integration of the increment of plastic energy density ΔW_{vp}, which is given by:

$$\begin{aligned}\Delta W_{vp}(\mathbf{x},\ t) &= \sum_{s=1}^{N_s} \tau^s(\mathbf{x},\ t)\Delta\gamma^s(\mathbf{x},\ t) = \sum_{s=1}^{N_s}\left[\tau^s_0(\mathbf{x},\ t) + \Delta\tau^s(\mathbf{x},\ t)\right]\Delta\gamma^s(\mathbf{x},\ t)\\ &= \sum_{s=1}^{N_s}\left[\tau^s_o(\mathbf{x},\ 0) + H\sum_{s=1}^{N_s}\gamma^s(\mathbf{x},\ t)\right]\Delta\gamma^s(\mathbf{x},\ t)\end{aligned}$$

$$= \overbrace{\tau_o^s(\mathbf{x},\ 0)}^{\text{constat}} \sum_{s=1}^{N_s} \Delta\gamma^s(\mathbf{x},\ t) + H\left[\sum_{s=1}^{N_s} \Delta\gamma^s(\mathbf{x},\ t)\right] \times \left[\sum_{s=1}^{N_s} \gamma^s(\mathbf{x},\ t)\right]$$
$$= \tau_o^s(\mathbf{x},\ 0) M(\mathbf{x}) \Delta\varepsilon_{vM}(\mathbf{x},\ t) + HM^2(\mathbf{x}) \left[\Delta\varepsilon_{vM}(\mathbf{x},\ t)\right] \times \left[\varepsilon_{vM}(\mathbf{x},\ t)\right] \tag{31}$$

in which the τ_o^s is the initial critical resolved shear stress (i.e. no strain hardening), and thus is a constant. Also, $M(\mathbf{x})$ denotes the Taylor factor, according to theory [28], that is defined as:

$$M(\mathbf{x}) = \Delta\gamma^s(\mathbf{x},\ t)/\Delta\varepsilon_{vM}(\mathbf{x},\ t). \tag{32}$$

Substituting Eq. (31) into Eq. (30) yields:

$$\begin{aligned} f_{vp}(\mathbf{x}) &= \int \Delta W_{vp}(\mathbf{x},\ t)dt \\ &= \int \tau_o^s(\mathbf{x},\ 0) M(\mathbf{x}) \Delta\varepsilon_{vM}(\mathbf{x},\ t) + HM^2(\mathbf{x}) \left[\Delta\varepsilon_{vM}(\mathbf{x},\ t)\right] \times \left[\varepsilon_{vM}(\mathbf{x},\ t)\right] dt \\ &= \tau_o^s(\mathbf{x},\ 0) M(\mathbf{x}) \int \Delta\varepsilon_{vM}(\mathbf{x},\ t)dt + 0.5HM^2(\mathbf{x}) \left[\int \Delta\varepsilon_{vM}(\mathbf{x},\ t)dt\right]^2 \\ &= \tau_o^s(\mathbf{x},\ 0) M(\mathbf{x}) \varepsilon_{vM}(\mathbf{x}) + 0.5HM^2(\mathbf{x}) \left[\varepsilon_{vM}(\mathbf{x})\right]^2. \end{aligned} \tag{33}$$

Substituting Eq. (29) into Eq. (33), the plastic energy takes the form of:

$$f_{vp}(\mathbf{x}) = \tau_o^s(0, \mathbf{x}) M(\mathbf{x}) \sum_g (-2\eta_g^3 + 3\eta_g^2) \varepsilon_{g,vM}(\mathbf{x},\ t) + 0.5HM^2(\mathbf{x}) \left[\sum_g (-2\eta_g^3 + 3\eta_g^2) \varepsilon_{g,vM}(\mathbf{x},\ t)\right]^2. \tag{34}$$

3.3. Elastic energy

The elastic energy of a polycrystalline material is defined as follows:

$$\begin{aligned} \mathcal{F}_{el} &= \int_V f_{el} dV = \int_V \frac{1}{2} C_{ijkl}(\mathbf{x}) \varepsilon_{ij}^e(\mathbf{x}) \varepsilon_{kl}^e(\mathbf{x}) dV \\ \mathcal{F}_{el}^r &= \int_V f_{el}^r dV = \int_V \frac{1}{2} C_{ijkl}^r(\mathbf{x}) \varepsilon_{ij}^e(\mathbf{x}) \varepsilon_{kl}^e(\mathbf{x}) dV \end{aligned} \tag{35}$$

where $\varepsilon_{ij}^e(\mathbf{x})$ denotes the local elastic strain tensor. For one specific material point, $C_{ijkl}(\mathbf{x})$ and $C_{ijkl}^r(\mathbf{x})$ denotes the elastic stiffness tensor contributed by deformed and recrystallization grains respectively, f_{el} and f_{el}^r represent the corresponding elastic energy density. Since the grains are rotated with respect to a fixed coordinate system, the elastic stiffness tensor for each grain is obtained by transforming the tensor with respect to the fixed coordinate system. Let C_{ijkl} represent the stiffness tensor for a single grain in a fixed reference frame. Then, the position-dependent elastic stiffness tensor for the entire polycrystal in terms of the order parameter fields is given by:

$$\begin{aligned} C_{ijkl}(\mathbf{x}) &= \sum_g \eta_g^2(\mathbf{x}) a_{ip}^g a_{jq}^g a_{kr}^g a_{ls}^g C_{pqrs} \\ C_{ijkl}^r(\mathbf{x}) &= \sum_g \phi_g^2(\mathbf{x}) a_{ip}^g a_{jq}^g a_{kr}^g a_{ls}^g C_{pqrs} \end{aligned} \tag{36}$$

where $\mathbf{a}$ is the transformation matrix representing the rotation of the coordinate system defined on a given grain 'g' with respect to the fixed reference frame. C_{pqrs} denotes the stiffness tensor of the reference medium. a_{ij} is expressed in terms of the symmetric Euler angles $\{\Psi,\ \Theta,\ \phi\}$ (Kocks convention) (in three dimensions):

$$\mathbf{a} = \begin{pmatrix} -\sin\phi \sin\Psi - \cos\phi \cos\Psi \cos\Theta & \sin\phi \cos\Psi - \cos\phi \sin\Psi \cos\Theta & \cos\phi \sin\Theta \\ \cos\phi \sin\Psi - \sin\phi \cos\Psi \cos\Theta & -\cos\phi \cos\Psi - \sin\phi \sin\Psi \cos\Theta & \sin\phi \sin\Theta \\ \cos\Psi \sin\Theta & \sin\Psi \sin\Theta & \cos\Theta \end{pmatrix}. \tag{37}$$

3.4. Kinetics of recrystallization

The time evolution of the order parameters is governed by kinetic equations relating time derivatives to the corresponding driving forces, defined as the functional derivatives (noted $\delta\mathcal{F}/\delta$) of $\mathcal{F}$ with respect to the fields. The Allen–Cahn equations are solved for the non-conserved order parameters of both the deformed grain and the recrystallized grain:

$$\frac{\partial \eta_q(\mathbf{x},t)}{\partial t} = -L\frac{\delta \mathcal{F}}{\delta \eta_q(\mathbf{x},t)} = -L(\mu_{ch}+\mu_{el}+\mu_{vp}) \tag{38}$$

$$\frac{\partial \phi_r(\mathbf{x},t)}{\partial t} = -L\frac{\delta \mathcal{F}}{\delta \phi_r(\mathbf{x},t)} = -L(\mu^r_{ch}+\mu^r_{el}) \tag{39}$$

where L is the kinetic rate coefficient relating to the grain boundary mobility M_0 and grain boundary energy σ_{gb}, and can be described as:

$$L = M_0 \times \sigma_{gb}/\kappa. \tag{40}$$

Also, the curvature driven forces for migration of grain boundaries $\mu_{ch} = \partial f_{ch}/\partial \eta_q$ and $\mu^r_{ch} = \partial f^r_{ch}/\delta\phi_r$, respectively corresponding to the deformed grain and the recrystallized grain are given as:

$$\begin{aligned}\mu_{ch}(\mathbf{x}) &= \frac{\partial f_0}{\partial \eta_g} - \kappa\nabla^2\eta_g \\ &= -\alpha\eta_g(\mathbf{x},t) + \beta\eta_g^3(\mathbf{x},t) + 2\gamma\eta_g(\mathbf{x},t)\sum_{s\neq g}\eta_s^2(\mathbf{x},t) + 2\gamma\eta_g(\mathbf{x},t)\sum_r \phi_r^2(\mathbf{x},t) - \kappa\nabla^2\eta_g(\mathbf{x},t)\end{aligned} \tag{41}$$

$$\begin{aligned}\mu^r_{ch}(\mathbf{x}) &= \frac{\partial f^r_0}{\partial \phi_r} - \kappa\nabla^2\phi_r \\ &= -\alpha\phi_r(\mathbf{x},t) + \beta\phi_r^3(\mathbf{x},t) + 2\gamma\phi_r(\mathbf{x},t)\sum_{s\neq r}\phi_s^2(\mathbf{x},t) + 2\gamma\phi_r(\mathbf{x},t)\sum_g \eta_g^2(\mathbf{x},t) - \kappa\nabla^2\phi_r(\mathbf{x},t).\end{aligned} \tag{42}$$

The elastic driven force μ_{el} (similar operation on μ^r_{el}) is obtained with the following derivation:

$$\mu_{el}(\mathbf{x}) = \frac{\partial f_{el}}{\partial \eta_g} = \frac{\partial f_{el}}{\partial \eta_g^2}\cdot\frac{\partial \eta_g^2}{\partial \eta_g} = 2\eta_g\frac{\partial f_{el}}{\partial \eta_g^2}. \tag{43}$$

Thus, the elastic driving forces μ_{el} and μ^r_{el} are given by:

$$\mu_{el}(\mathbf{x}) = \eta_g(\mathbf{x})a^g_{ip}a^g_{jq}a^g_{kr}a^g_{ls}C_{pqrs}\varepsilon^e_{ij}(\mathbf{x})\varepsilon^e_{kl}(\mathbf{x}) - 3\eta_g(\mathbf{x})(1-\eta_g(\mathbf{x}))C_{ijkl}(\mathbf{x})\varepsilon^e_{ij}(\mathbf{x})\varepsilon^p_{g,kl}(\mathbf{x}) \tag{44}$$

$$\mu^r_{el}(\mathbf{x}) = \phi_g(\mathbf{x})a^g_{ip}a^g_{jq}a^g_{kr}a^g_{ls}C_{pqrs}\varepsilon^e_{ij}(\mathbf{x})\varepsilon^e_{kl}(\mathbf{x}) \tag{45}$$

where $\eta_g(\mathbf{x})$ or $\phi_g(\mathbf{x}) = 1$ within grain 'g' and zero elsewhere. Similarly, the plastic driven force μ_{vp} is obtained as:

$$\begin{aligned}\mu_{vp}(\mathbf{x}) &= \frac{\partial f_{vp}}{\partial \eta_g} = \tau^s_o(0,\mathbf{x})M(\mathbf{x})\sum_g 6(-\eta_g^2+\eta_g)\varepsilon_{g,vM}(\mathbf{x},\ t) \\ &\quad + 0.5HM^2(\mathbf{x})\sum_g(24\eta_g^5 - 48\eta_g^4 + 36\eta_g^3)\left[\varepsilon_{g,vM}(\mathbf{x},\ t)\right]^2.\end{aligned} \tag{46}$$

3.5. Computational procedure

The detailed procedure to simulate the static recrystallization process of deformed polycrystalline systems using the present FFT-based phase-field model is given in the form of flowchart as illustrated in Fig. 3.

4. Numerical examples

In what follows we present two applications to assess the performance of the proposed FFT-based PFM taking the static recrystallization as an example. First, a simple case of a deformed single crystal is designed to validate the

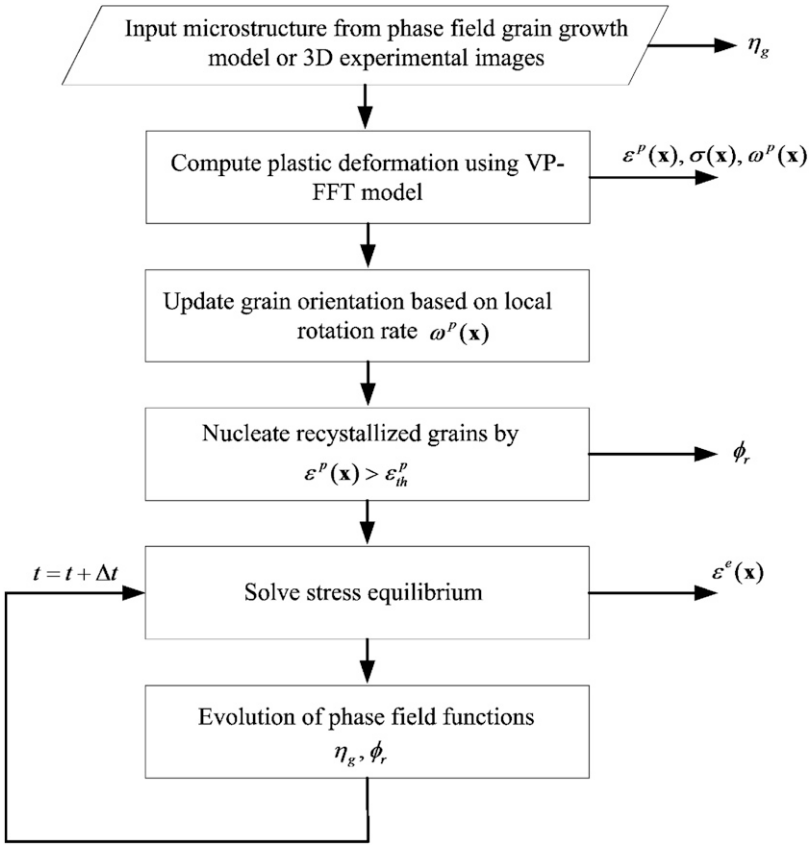

Fig. 3. Flow chart of the proposed FFT-based phase-field model to simulate static recrystallization.

recrystallization kinetics of the proposed model, by comparing the results obtained using the theoretical JMAK model. Next, we apply the proposed model to a more realistic case of a polycrystal with multiple deformed grains. Finally, we discuss the effect of applied strain on the recrystallization kinetics as well as the recrystallized grain size.

4.1. Validation of recrystallization kinetics

Our first verification test concerns a simple case with only one deformed single crystal ($G = 1$), thus producing a uniform distribution of plastic strain before recrystallization. An appealing feature of this problem is that it is amenable to an analytical solution of its recrystallization kinetics that comes from the JMAK equation [3,4]. In the JMAK model, random nucleation is assumed to occur either by site saturation or at constant nucleation rate. Here the case of site saturation is considered. Accordingly, randomly distributed nuclei are assumed. Five hundred nuclei are instantaneously seeded in the simulation domain. A uniform plastic driving force of 0.4 is assumed and the elastic driving force is neglected.

Computer simulations are performed on a cubic lattice with three system sizes by successively refinement, i.e. $64 \times 64 \times 64$, $96 \times 96 \times 96$ and $128 \times 128 \times 128$ grid points. $R = 500$ order parameters (recrystallized grains) are employed in this study. The values of the coefficients appearing in Eqs. (24) and (25) are: $\alpha = \beta = \gamma = 1$ and $\kappa = 1$. $L = 1$ is used in Eqs. (38) and (39). The lattice size Δx is set to 2.0, and a time step Δt of 0.05, 0.1, 0.3 are employed in the simulations. Periodic boundary conditions are employed.

Fig. 4 shows the 3-D microstructure evolution upon recrystallization under the JMAK assumptions with system size of $96 \times 96 \times 96$. The new grains grew spherically before they impinge on each other, which is consistent with the JMAK assumption of isotropic growth. At the end of the process, the new grains completely fill the domain and form polyhedral shapes. Fig. 5 shows the recrystallization kinetics plot obtained from our 3-D phase-field simulations. It is

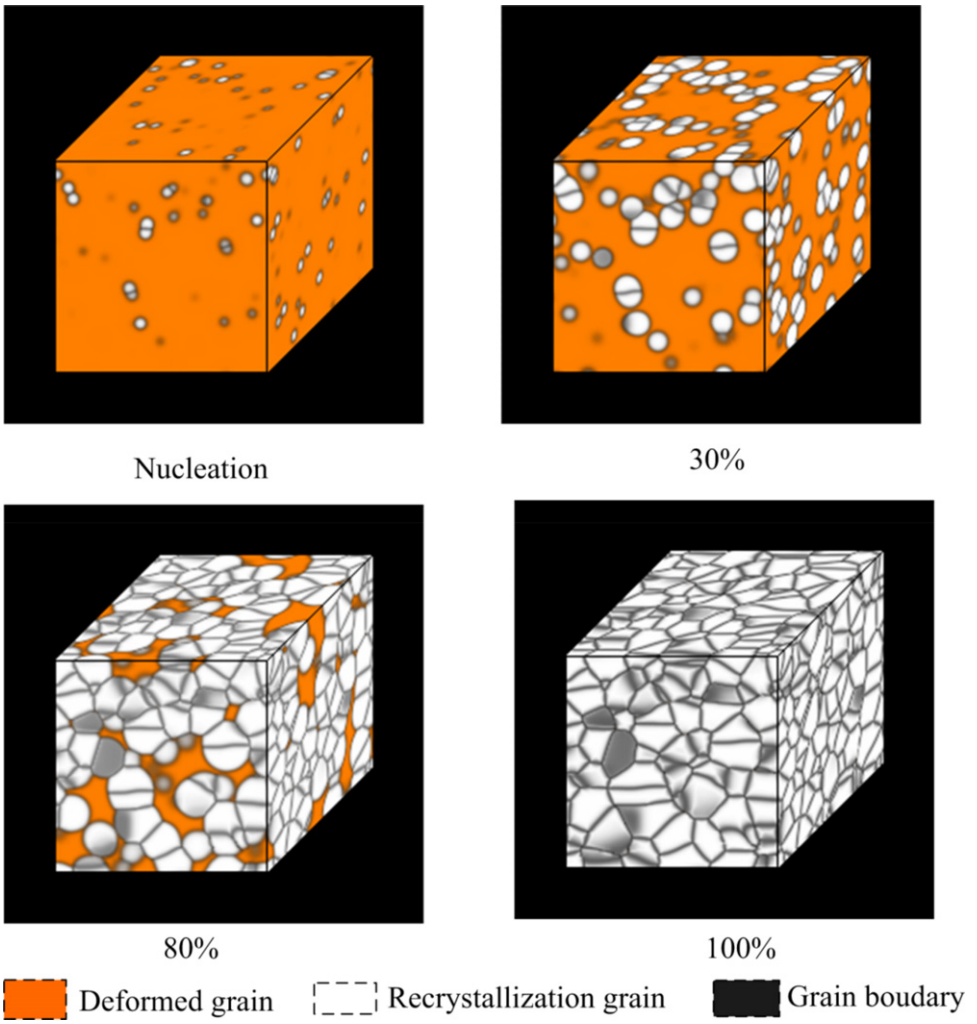

Fig. 4. Validation of recrystallization kinetics: 3-D microstructure evolution in the case of homogeneous nucleation and driving forces satisfying the JMAK assumption.

clearly observed that the exponent n of the present method exhibits excellent agreement with the theoretical JMAK value of 3, regardless of the system size considered, in spite of the imperfect linearity of the plotted lines. The JMAK exponent n is defined by the following equations [3,4]:

$$\begin{aligned} & X = 1 - \exp(-Kt^n) \\ & \Rightarrow \ln(-\ln(1-X)) = \ln(K) + n\ln(t) \end{aligned} \tag{47}$$

which yields a straight line with gradient n and intercept $\ln(K)$ in a $n(-\ln(1-X))$ vs. $\ln(t)$ plot, where X corresponds to the recrystallization volume fraction.

The sensitivity analysis, carried out here to demonstrate the stability of the method, shows that the exponent n converges to the corresponding JMAK analytical solution with decreasing the time step Δt as illustrated in Fig. 6.

4.2. Polycrystal recrystallization

Next, we consider a more interesting case of a polycrystal with multiple deformed grains, with a starting microstructure consisting of 225 grains ($G = 225$) generated by a phase-field grain growth simulation. [20], as shown in Fig. 2(a).

Simulations were performed on a cubic lattice with $64 \times 64 \times 64$ grid points. As before, $R = 500$ order parameters (recrystallized grains) are employed in this study. Δx is the lattice grid size, chosen to be 1 μm. The gradient energy

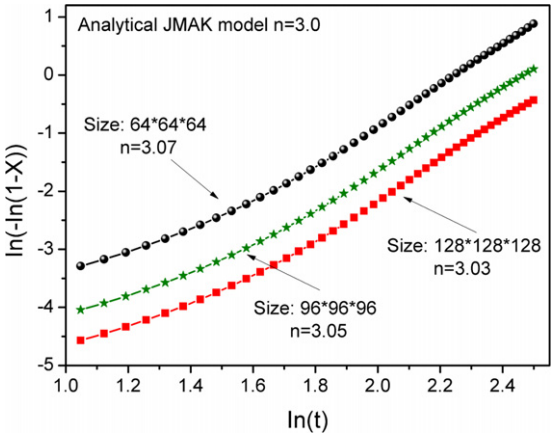

Fig. 5. JMAK plots of the simulated recrystallization kinetics.

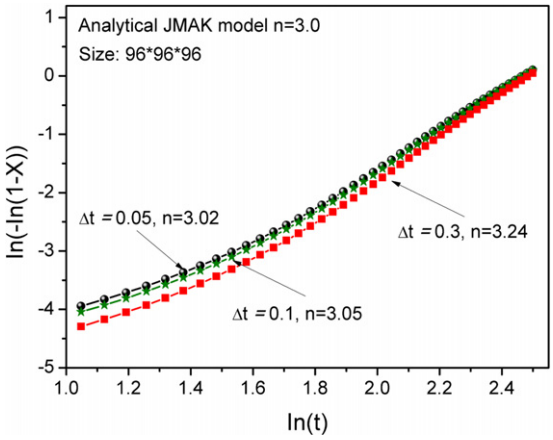

Fig. 6. Effect of the time step on the recrystallization kinetics.

coefficient κ associated with the grain order parameters is assumed to be 4.0×10^{-6} J m^{-1}. For the local free energy density described in Eqs. (24) and (25), we adopted $\alpha = \beta = \gamma = 1$, and, according to data available in the literature [47], a barrier height $h_b = 1.14 \times 10^6$ J m^{-3}. The equilibrium grain boundary energy σ_{gb} is 0.82 J m^{-2} and the equilibrium grain boundary width $l_{gb} = \sqrt{2\kappa/h_b}$ is 2.6 μm. These values are reasonable for generic high-angle grain boundaries. The kinetic coefficient L for the Allen–Cahn equation (Eq. (24)) is chosen to be 0.36×10^{-2} m^3 J^{-1} s^{-1}, and the intrinsic mobility M_0 of the grain boundary motion is taken as 1.76×10^{-8} m^4 J^{-1} s^{-1} using the relation in Eq. (40). The time step Δt for integration is taken as 0.56×10^{-4} s. The kinetic equations are solved in their dimensionless forms. The parameters are normalized by $\Delta x^* = \Delta x/l$, $\Delta t^* = L \times E \times \Delta t$, $h_b^* = h_b/E$, $k^* = k/E \cdot l^2$ and $M_0^* = M_0/L \cdot l^2$, where E is the characteristic energy (taken to be 10^6 J m^{-3}) and l is the characteristic length (taken to be 2 μm). All the simulations are conducted using periodic boundary conditions as before. The physical parameters and their normalized values are summarized in Table 1.

4.2.1. Plastic deformation from FFT viscoplastic model

In order to investigate microstructure evolution coupled to viscoplasticity during recrystallization, the first step is to predict the plastic strain field of the deformed microstructure using the CP-FFT model. The boundary conditions correspond to uniaxial tension along x_3 (see Fig. 2), with an applied strain rate component along the tensile axis $\dot{E}_{33} = 1$ s^{-1}. The CP-FFT simulation is carried out in 100 steps of 0.1%, up to a strain of 10%. The single crystal grains deform plastically by slip on 12 $\{1\ 1\ 1\}\langle 1\ 1\ 0\rangle$ slip systems with an initial CRSS value of $\tau_o^s = 11$ MPa and a stress exponent $n = 10$. Fig. 7(a) and (b) show, respectively, the von Mises stress and strain fields,

Table 1
Phase-field simulation parameters and their normalized values for recrystallization.

Parameter	Real value		Normalized value	
	Parameter	Value	Parameter	Value
Barrier height	h_b	1.14×10^6 J m^{-3}	$h_b^* = h_b/E$	1.14
Gain boundary energy	σ_{gb}	0.82 J m^{-2}	$\sigma_{gb}^* = \sigma_{gb}/(E \times l)$	0.41
Gradient energy coefficient	κ	4.0×10^{-6} J m^{-1}	$\kappa = \kappa/(E \times l^2)$	1
Grain order interaction	α, β, γ	1	$\alpha^*, \beta^*, \gamma^* = \gamma/\gamma$	1
Kinetic Coefficient	L	0.36×10^{-2} m^3 J^{-1} s^{-1}	$L^* = L/L$	1
Grain boundary mobility	M_o	1.76×10^{-14} m^4 J^{-1} s^{-1}	$M_o^* = M_o/L \cdot l^2$	2.25
Grid size	Δx	1 μm	$\Delta x^* = \Delta x/l$	0.5
Grain boundary width	l_{gb}	2.6 μm	$l_{gb}^* = l_{gb}/l$	1.3
Time step	Δt	0.56×10^{-4} s	$\Delta t^* = L \times E \times \Delta t$	0.2

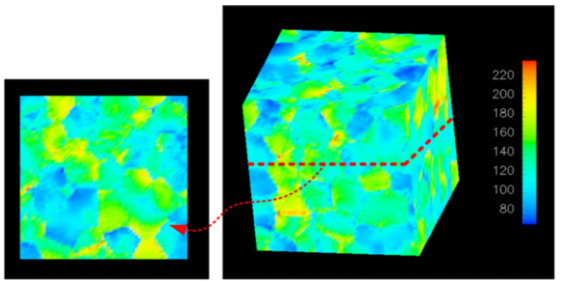

(a) von Mises stress.

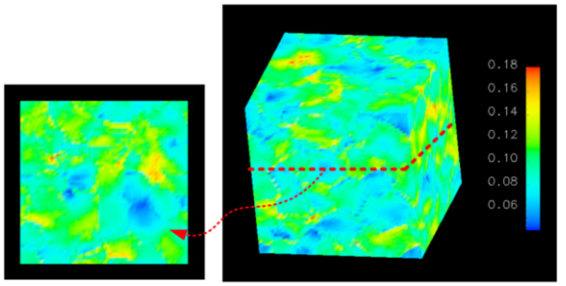

(b) von Mises strain.

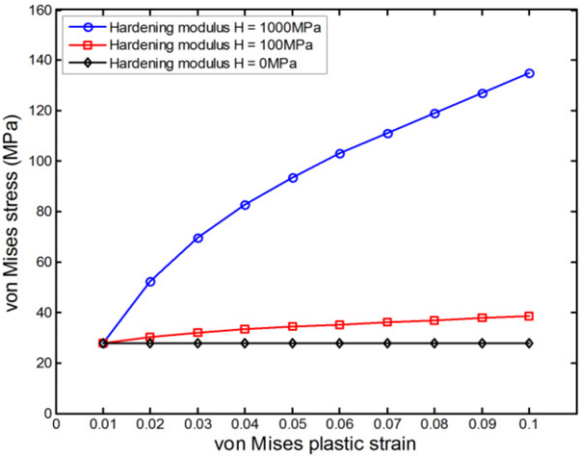

(c) Strain–stress curve.

Fig. 7. Plastic deformation calculated by the CP-FFT model: (a) local von Mises stress field; (b) local von Mises plastic strain field; (c) global strain–stress curve with these different hardening modulus values.

In addition, we studied the effect of strain-hardening, and four different values of the linear strain hardening modulus are employed : $H = 1000$ MPa, $H = 100$ MPa and $H = 0$ MPa. The relatively high strain-hardening dependence of the stress–strain curves is well captured by the model as shown in Fig. 7(c).

4.2.2. Nucleation criterion

In the second step, a simple criterion based on the site saturated nucleation conditions described in Section 2.3 is employed to identity the nucleation site of recrystallization. The threshold value of strain in Eq. (9) is chosen as 0.1. In order to investigate the effect of applied deformation, three different applied strains are utilized: 0.1, 0.05, and 0.025 with, respectively, 100, 50, and 25 steps of 0.1%. The hardening modulus of $H = 1000$ MPa is used in this step, and throughout the rest of sections.

Fig. 8 presents the microstructure with nucleation sites, for three different applied strains. The nucleation is found to occur at sites of high strain, as expected, which mostly correspond to the regions near the grain boundaries. In

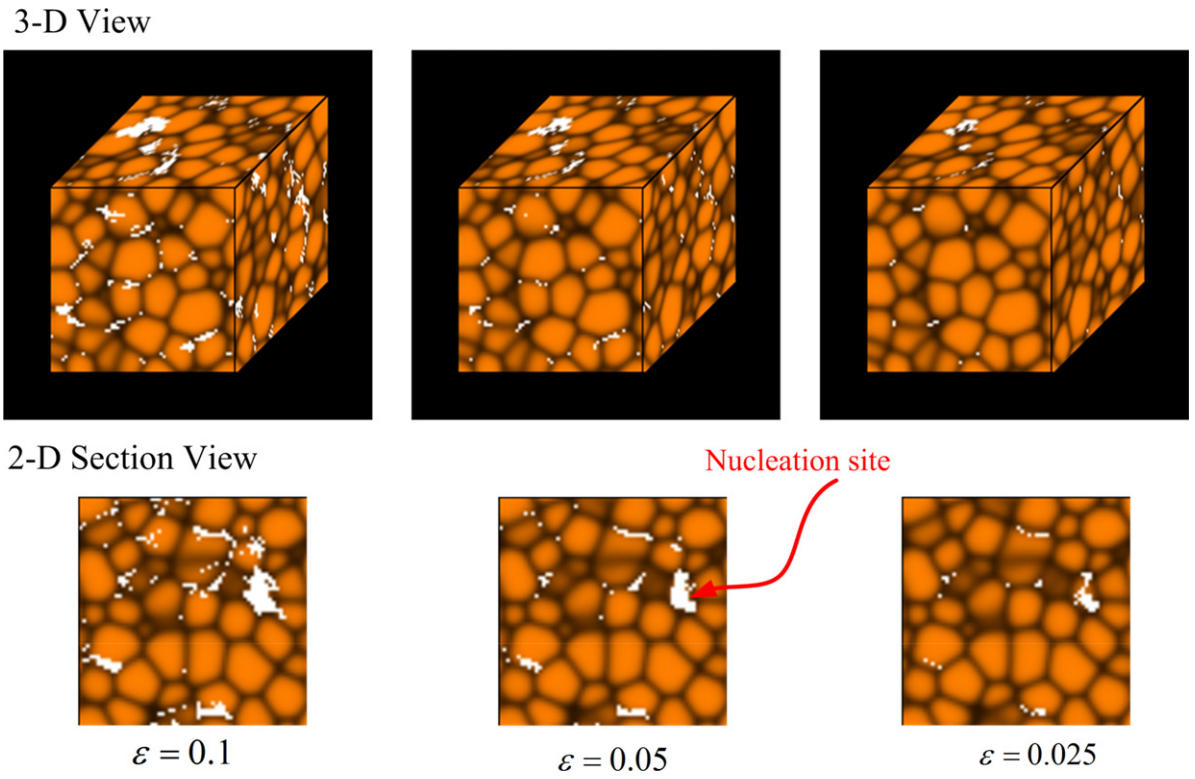

Fig. 8. Nucleation site under three different applied strains: 0.1, 0.05, and 0.025.

addition, it is observed that decreasing the applied strain results in a decrease of the number of nucleation sites for recrystallization.

4.2.3. Validation of stress equilibrium

As pointed out before, the stress equation is solved during each step of temporal phase-field evolution, for which, one fundamental issue is to verify the FFT-based solver in treating equilibrium, prior to phase-field evolution. For this purpose, a theoretical model [48] is employed to provide the reference solutions for comparison, as

$$\boldsymbol{\varepsilon}(\mathbf{x}) = \mathbf{C}^{-1} : \bar{\boldsymbol{\sigma}} + \bar{\boldsymbol{\varepsilon}}^{\mathrm{p}} + \beta(\boldsymbol{\varepsilon}^{\mathrm{p}}(\mathbf{x}) - \bar{\boldsymbol{\varepsilon}}^{\mathrm{p}}) \tag{48}$$

where $\beta = \frac{2(4-5\nu)}{15(1-\nu)}$, ν is the Poisson ratio.

For simplicity, an elastically isotropic system is chosen for the simulations, although the model is applicable to general, elastically anisotropic systems. The elastic moduli of the system are taken to be $C_{11} = 170.2$ GPa, $C_{12} = 114.9$ GPa and $C_{44} = 61.0$ GPa.

Fig. 9 compares the von Mises local elastic strain field after nucleation of recrystallization between our FFT-based solver and the theoretical model. It is observed the results from our FFT-based solver are clearly in good agreement with the theoretical ones, especially for the nucleation site, although a small difference is found in non-recrystallization regions. Here, we also need to keep in mind that our focus is on the migration of grain boundaries in the recrystallization region.

Another interesting phenomenon found in Fig. 9 is that the elastic strains are no longer negligible after nucleation of strain-free new grains, instead, they are comparable to the plastic ones, suggesting that stress equilibrium must be considered for each phase-field time step during recrystallization.

4.2.4. Recrystallization process

Fig. 10 shows time slices (snapshots) of the microstructure evolution during the recrystallization simulations in the case of applied strain of 0.1. The deformed grains are shown in orange, the recrystallized grains in white, and the grain

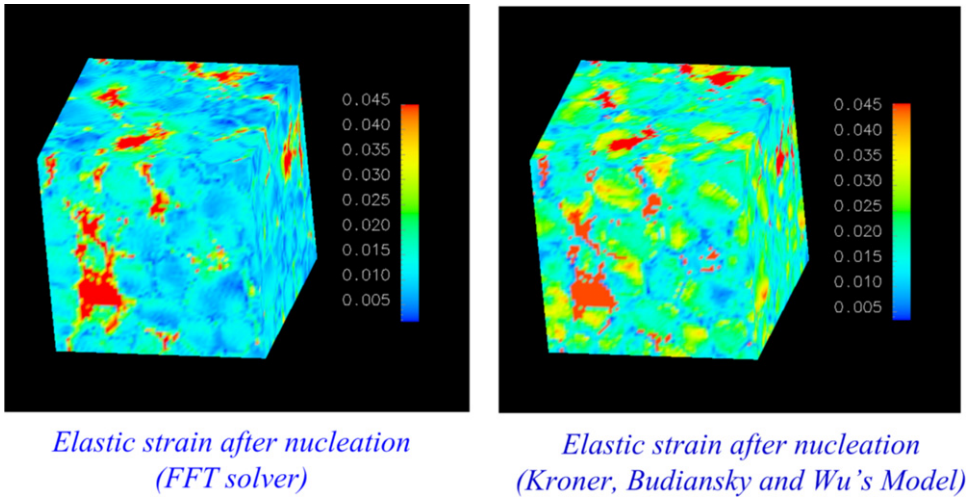

Fig. 9. Validation of stress equilibrium: comparison of local von Mises elastic strain field after nucleation between our FFT solver and the theoretical model [48].

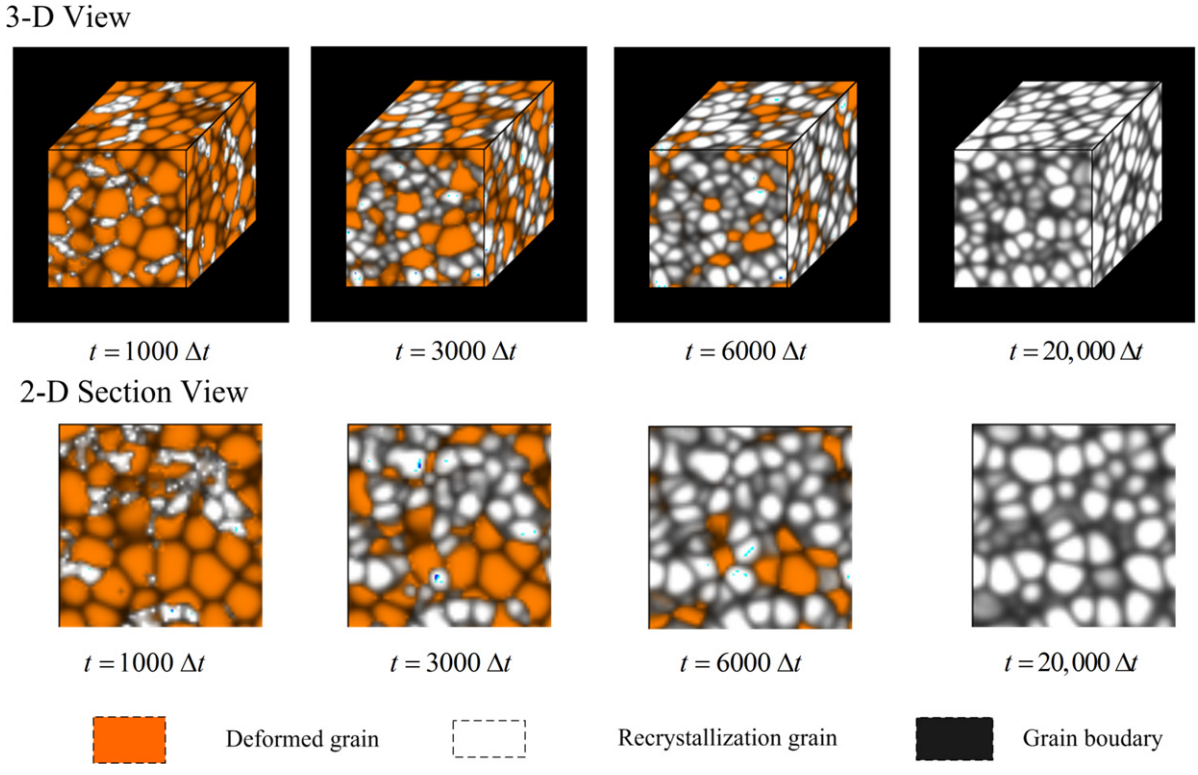

Fig. 10. Time slices of microstructure evolution during static recrystallization.

boundaries in black. Comparing Figs. 7(b) and 10, it can be seen that the recrystallized grains start to grow at sites with relatively high plastic strain, and spread into relatively low plastic strain regions. In particular, the 2-D sections show (a) grains in the upper left as well as in the middle right with relatively high stored energy, which are filled with nuclei at an early stage (3000 steps), and (b) delayed recrystallization in regions of relatively low stored energy, such as the lower left grains.

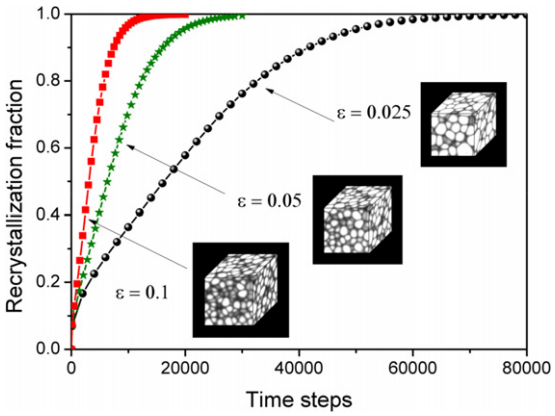

Fig. 11. Effect of applied strain on the recrystallization kinetics and the recrystallized grain size.

4.2.5. *Effect of applied strain*

The effect of applied strain on recrystallization kinetics and the recrystallized grain size is investigated. The corresponding results are plotted in Fig. 11. As expected, large applied plastic deformation speeds up the recrystallization process due to the large driving forces. Moreover, a remarkable tendency towards producing more refined recrystallized grains is observed as the applied strain increases. This might be related to the fact that larger applied strains imply the generation of more recrystallization nuclei, thereby giving rise to smaller recrystallized grain size. Animations of the whole recrystallization process, including recrystallized grain nucleation and growth under different applied plastic strains are included as Supplementary material (see Appendix A).

5. Conclusions

A new fast Fourier transform (FFT) based phase-field model (PFM) has been developed by integrating a micro-elastic PFM and a crystal plasticity (CP) model, and applied to 3-D static recrystallization of deformed polycrystals. The proposed model has been demonstrated by comparing the predicted recrystallization kinetics with the theoretical Johnson–Mehl–Avrami–Kolmogorov equation. It is found that increasing the plastic pre-deformation applied to the polycrystals accelerates the recrystallization process, and results in a decrease of recrystallized grain size.

We solved the stress equilibrium equation during each step of temporal phase-field evolution, which, to our knowledge, has never been considered in all existing grain growth and recrystallization models. Such implementation allows the phase-field method to simultaneously account for elastic and plastic driven forces, which have been found to coexist and interact during the grain growth and recrystallization process. More importantly, the proposed computational framework has the general character and is applicable to other plasticity-driven phase-field evolution processes, e.g. crystal growth, martensitic phase transformation, and electrochemical phase transformation.

Another important advantage of the present framework is the use of FFT solver in both models, which naturally guarantees their seamless integration. Furthermore, the intensive use of FFTs significantly enhances the computational efficiency of the method, especially for the 3-D cases, in comparison with CP-FEM for which the number of the elements that can be investigated is limited, i.e. far from being statistically representative, with presently available computational resources. In contrast, the proposed method is able to yield 3-D space-resolved predictions with high intragranular resolution, from which reliable statistical averages of kinetic and other parameters can be extracted.

Finally, of particular interest is the starting microstructure of the present method that can be either numerically-generated, e.g. from a PFM grain growth simulation, like in the case presented here, or obtained by means of 3-D experimental techniques. The latter would make possible to use the proposed method with a direct input from 3-D images of materials microstructures. The experiments, in turn, could be utilized to validate the modeling results, which is beyond the scope of this study, and will be reported in a forthcoming publication. On the disadvantage side, the requirement of periodic boundary conditions in Fourier space makes the FFT-based formulations less general than the FEM-base models. In addition, the small strain formulations in the CP models are not consistent with the experimental condition having a finite strain loading, therefore, the incorporation of finite strain formulations in the CP models [49] are necessary in the future.

Acknowledgments

This work is funded by the Center for Computational Materials Design (CCMD), a joint National Science Foundation (NSF) Industry/University Cooperative Research Center at Penn State (IIP-1034965) and Georgia Tech (IIP-1034968).

Appendix A. Supplementary material

Supplementary material related to this article can be found online at http://dx.doi.org/10.1016/j.cma.2014.12.007.

References

[1] S.-H. Choi, J.H. Cho, Primary recrystallization modelling for interstitial free steels, Mater. Sci. Eng. A 405 (2005) 86–101.
[2] F.J. Humphreys, M. Hatherly, Recrystallization and Related Annealing Phenomena, Elsevier, 1995.
[3] M. Avrami, Kinetics of phase change. I general theory, J. Chem. Phys. 7 (1939) 1103.
[4] M. Avrami, Kinetics of phase change. II transformation-time relations for random distribution of nuclei, J. Chem. Phys. 8 (1940) 212.
[5] B. Radhakrishnan, G. Sarma, T. Zacharia, Modeling the kinetics and microstructural evolution during static recrystallization—Monte Carlo simulation of recrystallization, Acta Mater. 46 (1998) 4415–4433.
[6] E.A. Holm, M.A. Miodownik, A.D. Rollett, On abnormal subgrain growth and the origin of recrystallization nuclei, Acta Mater. 51 (2003) 2701–2716.
[7] A. Rollett, Overview of modeling and simulation of recrystallization, Prog. Mater. Sci. 42 (1997) 79–99.
[8] D. Raabe, R.C. Becker, Coupling of a crystal plasticity finite-element model with a probabilistic cellular automaton for simulating primary static recrystallization in aluminium, Modelling Simul. Mater. Sci. Eng. 8 (2000) 445.
[9] D. Raabe, L. Hantcherli, 2D cellular automaton simulation of the recrystallization texture of an IF sheet steel under consideration of Zener pinning, Comput. Mater. Sci. 34 (2005) 299–313.
[10] H. Nguyen-Xuan, T. Hoang, V.P. Nguyen, An isogeometric analysis for elliptic homogenization problems, Comput. Math. Appl. 67 (2014) 1722–1741.
[11] L. Chen, N. Nguyen-Thanh, H. Nguyen-Xuan, T. Rabczuk, S.P.A. Bordas, G. Limbert, Explicit finite deformation analysis of isogeometric membranes, Comput. Methods Appl. Mech. Engrg. 277 (2014) 104–130.
[12] I. Steinbach, M. Apel, Multi phase field model for solid state transformation with elastic strain, Physica D 217 (2006) 153–160.
[13] W. Boettinger, J. Warren, C. Beckermann, A. Karma, Phase-field simulation of solidification 1, Annu. Rev. Mater. Res. 32 (2002) 163–194.
[14] L.-Q. Chen, Phase-field models for microstructure evolution, Annu. Rev. Mater. Res. 32 (2002) 113–140.
[15] T. Takaki, Y. Hisakuni, T. Hirouchi, A. Yamanaka, Y. Tomita, Multi-phase-field simulations for dynamic recrystallization, Comput. Mater. Sci. 45 (2009) 881–888.
[16] T. Takaki, Y. Tomita, Static recrystallization simulations starting from predicted deformation microstructure by coupling multi-phase-field method and finite element method based on crystal plasticity, Int. J. Mech. Sci. 52 (2010) 320–328.
[17] B. Zhu, M. Militzer, 3D phase field modelling of recrystallization in a low-carbon steel, Modelling Simul. Mater. Sci. Eng. 20 (2012) 085011.
[18] Y. Suwa, Y. Saito, H. Onodera, Phase-field simulation of recrystallization based on the unified subgrain growth theory, Comput. Mater. Sci. 44 (2008) 286–295.
[19] S. Hu, L. Chen, A phase-field model for evolving microstructures with strong elastic inhomogeneity, Acta Mater. 49 (2001) 1879–1890.
[20] C. Krill III, L.-Q. Chen, Computer simulation of 3-D grain growth using a phase-field model, Acta Mater. 50 (2002) 3059–3075.
[21] L.-Q. Chen, W. Yang, Computer simulation of the domain dynamics of a quenched system with a large number of nonconserved order parameters: the grain-growth kinetics, Phys. Rev. B 50 (1994) 15752.
[22] M. Koslowski, A.M. Cuitino, M. Ortiz, A phase-field theory of dislocation dynamics, strain hardening and hysteresis in ductile single crystals, J. Mech. Phys. Solids 50 (2002) 2597–2635.
[23] D. Rodney, Y. Le Bouar, A. Finel, Phase field methods and dislocations, Acta Mater. 51 (2003) 17–30.
[24] Y.U. Wang, Y. Jin, A. Cuitino, A. Khachaturyan, Nanoscale phase field microelasticity theory of dislocations: model and 3D simulations, Acta Mater. 49 (2001) 1847–1857.
[25] M.E. Gurtin, A gradient theory of single-crystal viscoplasticity that accounts for geometrically necessary dislocations, J. Mech. Phys. Solids 50 (2002) 5–32.
[26] G. Boussinot, A. Finel, Y. Le Bouar, Phase-field modeling of bimodal microstructures in nickel-based superalloys, Acta Mater. 57 (2009) 921–931.
[27] N. Zhou, C. Shen, M. Mills, Y. Wang, Contributions from elastic inhomogeneity and from plasticity to γ' rafting in single-crystal Ni–Al, Acta Mater. 56 (2008) 6156–6173.
[28] F. Roters, P. Eisenlohr, L. Hantcherli, D. Tjahjanto, T. Bieler, D. Raabe, Overview of constitutive laws, kinematics, homogenization and multiscale methods in crystal plasticity finite-element modeling: theory, experiments, applications, Acta Mater. 58 (2010) 1152–1211.
[29] X. Guo, S.-Q. Shi, X. Ma, Elastoplastic phase field model for microstructure evolution, Appl. Phys. Lett. 87 (2005) 221910, 1–3.
[30] R. Ubachs, P. Schreurs, M. Geers, Phase field dependent viscoplastic behaviour of solder alloys, Int. J. Solids Struct. 42 (2005) 2533–2558.
[31] T. Uehara, T. Tsujino, N. Ohno, Elasto-plastic simulation of stress evolution during grain growth using a phase field model, J. Cryst. Growth 300 (2007) 530–537.
[32] A. Yamanaka, T. Takaki, Y. Tomita, Elastoplastic phase-field simulation of self-and plastic accommodations in Cubic → tetragonal martensitic transformation, Mater. Sci. Eng. A 491 (2008) 378–384.

[33] A. Gaubert, Y. Le Bouar, A. Finel, Coupling phase field and viscoplasticity to study rafting in Ni-based superalloys, Phil. Mag. 90 (2010) 375–404.
[34] K. Ammar, B. Appolaire, G. Cailletaud, S. Forest, Combining phase field approach and homogenization methods for modelling phase transformation in elastoplastic media, Eur. J. Comput. Mech./Rev. Eur. Méc. Numér. 18 (2009) 485–523.
[35] K. Ammar, B. Appolaire, G. Cailletaud, S. Forest, Phase field modeling of elasto-plastic deformation induced by diffusion controlled growth of a misfitting spherical precipitate, Phil. Mag. Lett. 91 (2011) 164–172.
[36] R. Lebensohn, N-site modeling of a 3D viscoplastic polycrystal using fast Fourier transform, Acta Mater. 49 (2001) 2723–2737.
[37] R. Lebensohn, Y. Liu, P.P. Castañeda, Macroscopic properties and field fluctuations in model power-law polycrystals: full-field solutions versus self-consistent estimates, Proc. R. Soc. Lond. Ser. A Math. Phys. Eng. Sci. 460 (2004) 1381–1405.
[38] R. Lebensohn, Y. Liu, P. Ponte Castaneda, On the accuracy of the self-consistent approximation for polycrystals: comparison with full-field numerical simulations, Acta Mater. 52 (2004) 5347–5361.
[39] R.A. Lebensohn, R. Brenner, O. Castelnau, A.D. Rollett, Orientation image-based micromechanical modelling of subgrain texture evolution in polycrystalline copper, Acta Mater. 56 (2008) 3914–3926.
[40] R.A. Lebensohn, A.K. Kanjarla, P. Eisenlohr, An elasto-viscoplastic formulation based on fast Fourier transforms for the prediction of micromechanical fields in polycrystalline materials, Int. J. Plast. 32 (2012) 59–69.
[41] A. Prakash, R. Lebensohn, Simulation of micromechanical behavior of polycrystals: finite elements versus fast Fourier transforms, Modelling Simul. Mater. Sci. Eng. 17 (2009) 064010.
[42] H. Moulinec, P. Suquet, A numerical method for computing the overall response of nonlinear composites with complex microstructure, Comput. Methods Appl. Mech. Engrg. 157 (1998) 69–94.
[43] J. Michel, H. Moulinec, P. Suquet, A computational method based on augmented Lagrangians and fast Fourier transforms for composites with high contrast, CMES Comput. Model. Eng. Sci. 1 (2000) 79–88.
[44] J. Michel, H. Moulinec, P. Suquet, A computational scheme for linear and non-linear composites with arbitrary phase contrast, Internat. J. Numer. Methods Engrg. 52 (2001) 139–160.
[45] S. Bhattacharyya, T.W. Heo, K. Chang, L.-Q. Chen, A phase-field model of stress effect on grain boundary migration, Modelling Simul. Mater. Sci. Eng. 19 (2011) 035002.
[46] B.S. Anglin, R.A. Lebensohn, A.D. Rollett, Validation of a numerical method based on fast Fourier transforms for heterogeneous thermoelastic materials by comparison with analytical solutions, Comput. Mater. Sci. 87 (2014) 209–217.
[47] T.W. Heo, S. Bhattacharyya, L.-Q. Chen, A phase field study of strain energy effects on solute–grain boundary interactions, Acta Mater. 59 (2011) 7800–7815.
[48] B. Budiansky, T.T. Wu, Theoretical prediction of plastic strains of polycrystals, in, DTIC Document, 1961.
[49] P. Eisenlohr, M. Diehl, R. Lebensohn, F. Roters, A spectral method solution to crystal elasto-viscoplasticity at finite strains, Int. J. Plast. 46 (2013) 37–53.